Trapping of biological macromolecules in the three-dimensional mesocage pore cavities of monolith adsorbents

**M. A. Shenashen · Sherif A. El-Safty ·
M. Khairy**

Abstract Gene technology is experiencing remarkable progress, and proteins are becoming crucial in the field of disease diagnosis and treatment. Adsorption of biomolecules on the surface of inorganic materials is an important technique for diagnostic assays and gene applications. In this study, highly ordered mesocage cubic Pm3n aluminumsilica monoliths were fabricated by the one-pot direct-templating of a microemulsion of the liquid crystalline phases of a Brij 56 surfactant. Mesocage cubic Pm3n aluminosilica monoliths with well-defined mesostructures offer high adsorption and loading capacity of proteins from an aqueous solution. Three-dimensional monoliths characterized by spherical pore cavities can potentially perform efficient adsorption and trapping of insulin, cytochrome C, lysozyme, myoglobin, β-lactoglobin proteins. A wide variety of characterization techniques such as SAXS, SEM, TEM, the Brunauer–Emmett–Teller method for nitrogen adsorption and surface area measurements, and TEM were used. The adsorption of proteins as well as the kinetic and thermodynamic characteristics of adsorption was studied, and adsorption isotherms were described by the Langmuir equation. Our findings indicated that monolayer coverage of proteins formed on mesoporous adsorbent surfaces during immobilization and uptake assays. Adsorption efficiency of proteins was attained after a number of reuse cycles, which indicates the presence of mesoporous adsorbents of biomolecules. Integration of mesoporous adsorbents may be feasible in various scientific fields such as nanobioscience, material science, artificial implantation, protein purification, biosensors, drug delivery systems, and molecular biology/biotechnology.

Keywords Protein · Mesocage cavities · Trapping · Three-dimensional aluminosilica · Monoliths · Adsorption

1 Introduction

The urgent demand for biological adsorbents for protein has resulted in increased interest in the use of inorganic materials as mesoporous adsorbents of biomolecules. The adsorption process of biological macromolecules is significant in diagnostic assays as well as fields such as gene and pharmaceutical sciences. A mesoporous adsorbent is expected to have the following advantages: stability during the adsorption process, reusability, low maintenance costs, high efficiency, and ease of operation assays [1–3]. Based on protein building, some side chains are hydrophobic whereas others are more hydrophilic [4]. Andrade et al. [5] mentioned that proteins are not homogeneous particles, which indicates that not all collision parts are equally effective in adsorption. The different tendencies for surface denaturation of proteins are due to the fact that different proteins face contacting points as well as to different interaction energies with the protein, such as hydrophobicity, hydrophilicity, and positively and negatively charged faces [5].

Several studies use nanostructures to separate biomolecules such as nickel oxide, multifunctional magnetic nanorods, different cores/shells, and porous materials [4]. Protein

M. A. Shenashen · S. A. El-Safty (✉) · M. Khairy
National Institute for Materials Science (NIMS), 1-2-1 Sengen, Tsukuba-shi, Ibaraki-ken 305-0047, Japan
e-mail: sherif.elsafty@nims.go.jp; sherif@aoni.waseda.jp

M. A. Shenashen
Egyptian Petroleum Research Institute (EPRI), Nasr City, Cairo, Egypt

S. A. El-Safty · M. Khairy
Graduate School for Advanced Science and Engineering, Waseda University, 3-4-1 Okubo, Shinjuku-ku, Tokyo 169-8555, Japan

uptake on the substrate follows a complex mechanism that involves numerous events such as conformational changes, hydrogen bonding, and/or hydrophobic and electrostatic interactions. Protein adsorbs at different qualities, conformations, and orientations depending on the chemical and physical characteristics of both the protein and the supported surfaces [1, 2]. Hierarchical mesoporous structures are ideal materials that have a large surface area, high porosity characterized by uniform and tunable mesopores, a hydrophilic character, and relatively good chemical and mechanical stability during changes in the microenvironment [6–8]. These features indicate that mesoporous materials are potential substrates for hosting catalysts, adsorbing proteins, constructing biosensors, separation, sensors, and fuel cells [6, 8–10]. Functional metal nanoparticles (NPs)-supported mesoporous oxide powder hosts are also potential materials because of their high surface area and continuous pore structure. Active alumina with mesostructures is an adsorbent material that supports a large number of catalysts [11]. Mesoporous Ni–alumina catalysts were synthesized and were found to exhibit well-developed framework porosity [12]. According to Xu and Gao, different functional proteins can bridge SiO_2 nanoparticles via charge attraction and hydrogen bonding, and then aggregate the nanoparticles into coralloid forms [13]. Despite these developments, designing mesostructures that are capable of macromolecule immobilization and uptake into the interior mesoporosity remains a challenge. To control the design of macromolecule adsorbent-based mesostructures, mesopore size is a crucial factor in protein penetration onto mesopores. Among all mesostructures, three-dimensional (3D) cage pore cavities have been receiving greater attention than one-dimensional or two-dimensional (2D) structures such as MCM-41 and SBA-15 in terms of mass transfer and pore blocking [9].

Lundqvist et al. [14] reported adsorption of human carbonic anhydrase variants onto silica nanoparticles of varying sizes and observed a larger perturbation of protein secondary structure on particles with larger diameters. This study suggests that unlike larger particles, smaller nanoparticles promoted retention of a native-like protein structure and function; this may be due to higher surface curvature. HCAI adsorption on silica nanoparticles with diameters of 6, 9, and 15 nm exhibits size-dependent behavior [14]. In another study on lysozyme adsorption onto silica nanoparticles with a diameter that ranges from 4 to 100 nm, the structure of the adsorbed layer and the activity of surface adsorbed lysozyme depend on the size of the nanoparticle [15]. Encapsulated proteins on organically modified silica are also more susceptible to surface hydration changes because of the proximity of alkyl chain groups [16]. El-Safty [17] fabricated hexagonal mesocylinder silica structures inside anodic alumina membrane (AAM) nanochannels, which were then used as nanofilter membranes for size exclusion separation

of proteins. The size-selective adsorption of low-molecular-weight proteins onto mesoporous silica materials may be used in protein encapsulation because of the critical pore sizes of these proteins [18, 19]. The preparation of highly active and stable mesoporous adsorbents of biomolecules is also a key requirement for achieving successful applications.

A unique self-assembly process exists between the surfactants and the inorganic precursors. The templating strategy that involves supramolecular arrays of organic amphiphiles is commonly used to prepare a variety of ordered 2D and 3D mesoporous architectures with a wide range of pore sizes as well as particle shapes and sizes. However, the structural properties of the structure-directing agents, surfactants, and the synthesis conditions' "composition domains" are crucial for controlling the physical characteristics of resultant mesoporous materials [20, 21]. A two-step method is commonly used to fabricate mesoporous aluminosilicas under mild acidic/basic conditions. However, this method has the following drawbacks [20]: (1) labor-intensive or complicated strategies that involve high temperature and long-term growth conditions, (2) uncontrolled phase geometries (2D or 3D) in final replicas, and (3) distortion of the mesostructures with high aluminum content in the frameworks.

Fabrication of aluminosilica mesostructures through direct templating of lyotropic/microemulsion liquid crystals can reliably control the actual microstructure phase of the templates and of final composite replicas such as gels, cast monoliths, or membranes [22]. An instant, one-pot synthesis (in the order of minutes) with simple composition domains can be used to fabricate aluminosilica molecular sieves in shape- and size-selective mesopore monoliths that exhibit high acidity, thereby achieving structural integrity and hydrothermal stability. Nanomaterials that exhibit such features can be instrumental in the development of new nanoscale membrane applications such as cracking catalysts, heavy metals, or organic adsorbents [22]. Therefore, the development of a new strategy that produces synthetically constructed mesostructures with tunable pore sizes throughout a 3D mesocage is necessary for protein adsorption. To understand better protein adsorption assay, efficient analytical methods and advanced biological application systems need to be developed. In this study, the simple, one-pot fabrication of low-cost mesocage cubic *Pm3n* aluminosilica monoliths with large surfaces area and uniform mesocage pores was performed. The 3D pores, mesocage cavities, and functional active surface that contained aluminum in the monoliths produced high-performance mesoporous adsorbents for biomolecules. These adsorbents exhibited enhanced adsorption capacity. This study also examined the main factors that affected the adsorption/trapping process. The reusability of mesoporous adsorbent monoliths in adsorption assays was also determined. Satisfactory immobilization and uptake assays onto the

mesoporous materials indicated applicability in the field of biology as well as in the encapsulation and trapping of proteins, bioanalysis, and drug delivery systems.

2 Materials and methods

2.1 Materials

All materials were used without further purification. Brij 56 surfactants $(C_{16}H_{33}(OCH_2CH_2)_{10}OH)$, tetramethylorthosilicate (TMOS), aluminum nitrate enneahydrate $Al(NO_3)_3.9H_2O$, insulin (INS; MW = 5.733 kDa, size = 2.4 nm), cytochrome C (CytC; MW = 12.327 kDa, size = 3.0 nm), lysozyme (LYS; MW = 14.3 kDa, size = 3.2 nm), myoglobin (Mb; MW = 16.95 kDa, size = 4.0 nm), and β-lactoglobin (β-LG; MW = 18.4 kDa, size = 4.2 nm) were obtained from Sigma-Adrich Company Ltd., USA. Dodecane was obtained from Wako Company Ltd., Osaka, Japan.

2.2 Synthesis of mesocage cubic *Pm3n* aluminosilica adsorbent

The one-pot synthesis of *Pm3n* aluminumsilica monoliths with different molar ratios of Si/Al was conducted by adopting instant direct-templating of a microemulsion of the liquid crystalline phases of Brij 56 surfactant. A monolith is typically defined as a geological feature such as a mountain, or a structure that consists of a single massive stone or rock (Scheme 1). In the direct synthesis of cubic *Pm3n* aluminosilica at an Si/Al mole ratio of 9 and at an TMOS/Brij-56 mass ratio of 0.5 (w/w), the precursor solution (1.125 g of Brij-56, 0.5625 g of dodecane, 2.25 g of TMOS, 0.64 g of Al (NO₃)₃, 2.813 g of H₂O–HCl (pH 1.3) was stirred for 5 min to form a homogenous sol–gel solution. The mass ratio of surfactant to dodecane was maintained at 2:1 for all syntheses of the mesoporous aluminosilica. To obtain samples with Si/Al sample ratios of 9, 4, 1.5, and 0.66, Al (NO₃)₃ content was varied and TMOS was maintained at 2.25 g. As hydrolysis/condensation reactions continued during evaporation, liquid viscosity of the material increased, methanol was removed using a diaphragm vacuum pump (DIVAC 1.2 L) connected with a rotary evaporator at 45 °C, and the resulting viscous liquid changed into an optical gel-like material (solid product) and acquired the shape and size of a round-balloon flask. Note, the mesocage cubic Pm3n mesoporous silica could be fabricated with the same synthesis protocol in terms of composition and condition, and in the absence of Al sources [i.e., without addition of Al(NO₃)₃]. To obtain macroscopic, crack-free, and shape-controlled silica translucent monoliths of a certain size, the translucent

glassy material was collected after 10 min evacuation. The drying process was completed at 40 °C for 24 h. Organic moieties were removed by calcination at 550 °C in air for 5 h [24]. Calcined material clearly possessed stable and tough material; however, the transparency of the monoliths was eliminated (see below).

2.3 Analysis of mesoporous aluminosilica monolith adsorbents

The particle size of the solid sample significantly affects analysis. The effect of the size and inhomogeneous distribution can be minimized by grinding the monolith into fine powder. Therefore, the monolith was ground into very fine gravel to obtain the desired surfaces for material analyses.

Small angle powder X-ray diffraction (XRD) patterns were measured by using a 18 kW diffractometer (Bruker D8 Advance) with monochromated CuKα radiation and with scattering reflections recorded for 2θ angles between 0.1° and 6.5° corresponding to *d*-spacing between 88.2 and 1.35 nm. The diffraction data were analyzed using the DIFRAC plus evaluation package (EVA) software with PDF-2 Release 2009 databases provided by Bruker AXS. The standard diffraction data were identified according to the databases of the International Centre for Diffraction Data (ICDD). For poor quality diffraction data, the TOPAS package program provided by Bruker AXS 2009 for profile and structure analysis was applied to integrate various
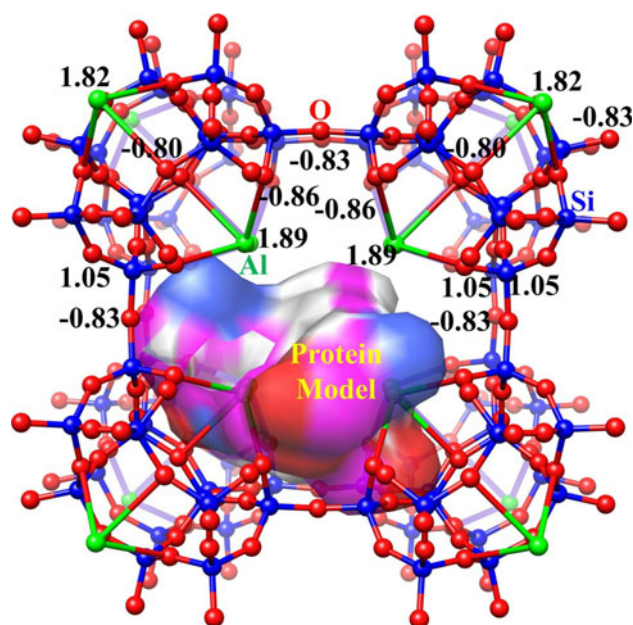
Scheme 1 Atomic charge distributions of 3D cubic *Pm3n* network clusters for 12 U of AlSi₄O₁₀ composition were calculated by the semiempirical PM3 method implemented on the HyperChem 8.0.7 program package (developed by Hypercube, Inc.). Si/Al ratio in this cluster is 4

types of XRD analyses by supporting all profile fit methods currently employed in powder diffractometry.

N₂ adsorption–desorption isotherms were measured using a BELSORP MIN-II analyzer (JP. BEL Co. Ltd) at 77 K. The pore size distribution was determined from the adsorption isotherms by using nonlocal density functional theory (NLDFT) on the basis of a spherical pore model. In addition, the pore size distribution calculated from the desorption branches of nitrogen isotherms is drastically different, which confirms the cavitation-controlled mechanism of evaporation [25, 26]. Specific surface area (S_{BET}) was calculated using multi-point adsorption data from linear segment of the N₂ adsorption isotherms using Brunauer–Emmett–Teller (BET) theory. Before the N₂ isothermal analysis, all prepared samples were pre-treated at 200 °C for 8 h under vacuum until the pressure was equilibrated to 10^{-3} Torr.

FESEM images were measured by a field-emission scanning electron microscopy (Hitachi S-4300). Before insertion into the chamber the powder substrates were fixed on a SEM stage using carbon tapes. The Pt films were deposited on substrates at room temperature by using an ion-sputter (Hitachi E-1030). The distance between the target and the substrate was 5.0 cm. The sputtering deposition system used for the experiments consists of a stainless steel chamber, which was evacuated down to 8×10^{-5} Pa with a turbo molecular pump backed up by a rotary pump. Before sputtering deposition, the Pt target (4 in. diameter, purity 99.95 %) was sputter cleaned in pure Ar. The Ar working pressure (2.8×10^{-1} Pa), the power supply (100 W) and the deposition rate were kept constant throughout these investigations. Moreover, to better record the SEM images of samples, the SEM micrographs were operated at 20 keV. Energy dispersive X-ray micro-analyzers (EDX) were recorded by employing Horiba EDS-130S, which directly connected with Hitachi FE-SEM S-4300. Elemental mapping of all the aluminosilica samples was carried out with the energy dispersive X-ray micro-analyzers with an acceleration voltage of 30 kV. Ten distinct spots were analyzed per sample, which resulted in 99 % confidence bounds of ±0.01 in the molar fraction of each cation (with their sum normalized to unity).

High-resolution transmission electron microscopy (HR TEM) was performed using a JEOL JEM model 2100F microscope. HRTEM was conducted at an acceleration voltage of 200 kV to obtain a lattice resolution of 0.1 nm. The HRTEM images were recorded using a CCD camera. TEM was carried out at a camera length of 80 cm and a spot size of 1 nm. The sample was dispersed in ethanol solution using an ultrasonic cleaner, and then dropped on a copper grid. Prior to inserting the samples in the HRTEM column, the grid was vacuum dried for 20 min.

Fourier transform infrared spectra (FTIR) were recorded by using an FTIR Prestige-21 (Shimadzu, Japan).

Batch adsorption of proteins onto the mesocage cubic *Pm3n* aluminosilicate monoliths was conducted in an aqueous solution. Adsorption assays were performed using a thermostatted shaker, and the rate of shaking was kept constant. After a set time interval, the container was removed from the thermostat and adsorption was quenched quickly by suction. No filtrated or centrifuging systems were used for the adsorption process because an uncrushed monolithic adsorbent was used. As a result, kinetic studies were conducted easily. The concentration of adsorbate solutes was measured on a Shimadzu 3700 model solid-state UV spectrophotometer. All adsorption experiments were conducted at room temperature (25 °C).

3 Results and discussion

3.1 Structural and textural features of mesocage bioadsorbent

The XRD profiles (Fig. 1a) of calcined mesoporous aluminosilicate reflect the high quality of the materials. The XRD pattern revealed three resolved high-intensity reflection peaks (Fig. 1a) with respective d-spacing ratios of $\sqrt{4}:\sqrt{5}:\sqrt{6}$, which indicated the 3D architecture ordering of primitive phases with m3m or m3n point groups. The low resolution of these diffraction lines indicated that the XRD profile can sufficiently identify primitive cubic Pm3n symmetry. The low resolution of these diffraction lines showed well-resolved reflection peaks with d-spacing ratios of $\sqrt{8}:\sqrt{12}:\sqrt{20}$ assigned to the (220), (222), and (420) reflections, respectively. The XRD data of solid aluminosilicate indicated highly ordered structures for the cubic crystallographic space group Pm3n, with a large unit cell dimension of ≈ 12.7 nm (Fig. 1a) [22, 23]. Despite the high loading level of adsorption of protein molecules onto the pore surface, finely resolved Bragg diffraction peaks were clearly observed for the cubic *Pm3n* mesoporous adsorbent with Si/Al ratios ≤ 4 (Fig. 1A(a, b). Retaining the mesoscopical orientation of the mesoporous adsorbent may lead to successful adsorption of different adsorbates especially protein molecules into condensed framework pore matrices of the 3D cubic mesostructures. However, the stability of the mesoporous matrices, which included those with high Al content (Fig. 1A(c, d), increased the possibility of high flux and uptake of the protein adsorption process. The partial collapse of mesostructures may be due to a lack of long-range crystallographic order or to finite size effects of Al–SiO₂ inside the mesopore structures, as evidenced by low-intensity reflections with high Al content [29, 30].

Electronic structures were calculated to determine charge distribution on each atom and the effect of Al sites on acidity.

Fig. 1 XRD (**A**) and N_2 isotherms (**B**) of cage cubic Pm3n aluminosilica adsorbents with a wide range of Si/Al ratios (w/w) of 9 (*a*), 4 (*b*), 1.5 (*c*), and 0.66 (*d*). *Inset* (**A**) displays the d-spacing, *hkl*, and 2-theta values of the diffraction peaks of aluminosilica adsorbents with Si/Al ratio of 9 (*a*). *Inset* (**B**) displays the BET surface area (S_{BET}), NLDFT mesopore size (*D*), and pore volume (*Vp*)
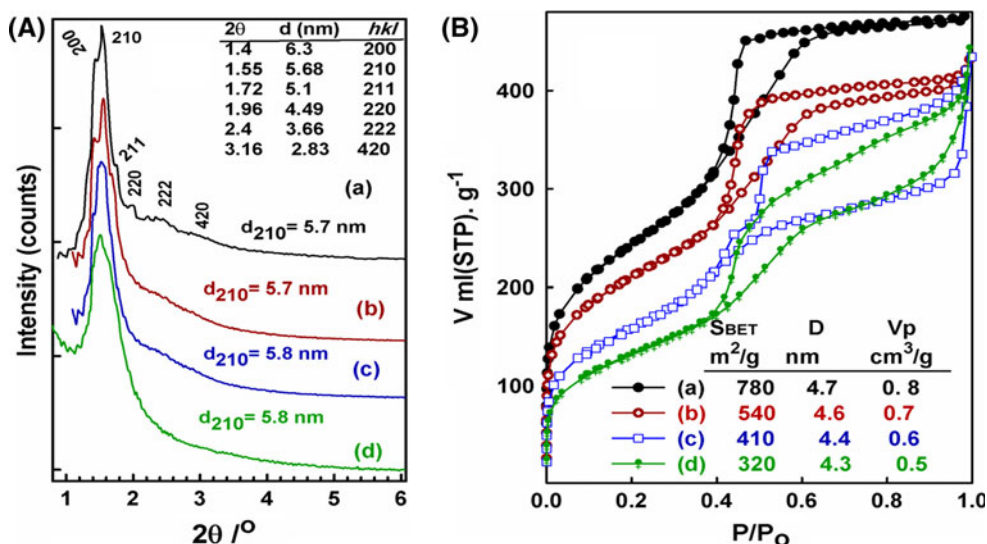
Calculations were performed using a semiempirical method (Scheme 1). The structural formation was proposed based on the cluster model of spherical aluminosilicates ($AlSi_4O_{12}$), which consisted of two types of oxygen linkages (oxygen-bonded to Si or Al and siloxane species), as a result of the interaction between silica and alumina sources. The results showed that the oxygen atoms in the Si–O–Al linkages were more negative than other oxygen atoms in the linkage species, which indicated a high number of acid sites. Al atoms had different charges depending on their position on the surface or towards the pore. According to our calculations, the Al charges were 1.89 and 1.82 on the surface and pore, respectively, which produced Brönsted and Lewis acidity followed by interaction with the heteroatoms of protein molecules (Scheme 1).

A high specific surface area is required for immobilization of elevated proteins. The nitrogen adsorption–desorption isotherms for different *Pm3n* monolith samples exhibited type IV behavior per the IUPAC classification, as well as pronounced hysteresis loops of H_2 types with the well-known sharp inflection of the adsorption/desorption branches that feature uniform and regular cage pore architectures (Fig. 1B) [17, 31]. Such cage structures were discussed in other reports [24]. These results can be attributed to capillary condensation within a narrow range of tubular pores. Increased aluminum content causes adsorption isotherms to shift toward a higher relative pressure (P/P_o). However, adsorption volume uptake was significantly decreased. Based on the N_2 isothermal results, the retention of the physical characteristics of the cubic *Pm3n* monoliths, such as large porosity, specific surface area, and pore volume, allow the protein molecules to access the monoliths. The cumulative pore volume and pore size distribution are directly affected by Si/Al ratios and the position of the Al content in the pore surfaces of frameworks. The slight

decrease in the spherical cavity of monoliths may be attributed to the increased Al content (i.e., decreased Si/Al ratio) in the frameworks, which leads to instability of aluminum in the monolith framework. However, during the dealumination process with calcination of high Al aluminosilicas with high Al content, aluminum may migrate to the framework surface to form a separate aluminum species. Retention of the orderly organized structures of aluminosilica may facilitate homogenous diffusion and rapid transport of protein molecules. The direct fabrication method of mesoporous adsorbents produces a wide range of pore sizes, which then leads to immobilization of a sizeable number of macromolecules [27].

These 3D cubic aluminosilica monoliths with pore cavities and active acid sites can potentially remove proteins from an aqueous solution. The coordination state of the aluminum species was investigated by ^{27}Al NMR (Fig. 2). In all aluminosilica samples, two ^{27}Al peaks were centered at the chemical shift of −1 and 58 ppm, which indicates the existence of octahedral (Al^{VI}, AlO_6, extra framework) and tetrahedral (Al^{IV}, AlO_4, framework) aluminum sites, respectively. Coordination and location of aluminum sites in the frameworks are instrumental in generating surface acidity of aluminosilica monoliths, which enhanced the protein's adsorption capacity. However, the functional aluminum active sites of four- or six-coordinate species contribute to adsorbate molecule binding (see below). The number of acid sites increased with the amount of aluminum, as shown by the increased Al^{IV}/Al^{VI} ratios (Fig. 2 insets). Enhanced surface acidity may result in strong interaction between the surface functional groups of the adsorbents and the proteins in an aqueous solution.

Figure 3 shows the main peaks in the FTIR spectra reflecting Al–OH, Al–O and Si–O functional groups in the high frequency stretching and low frequency bending
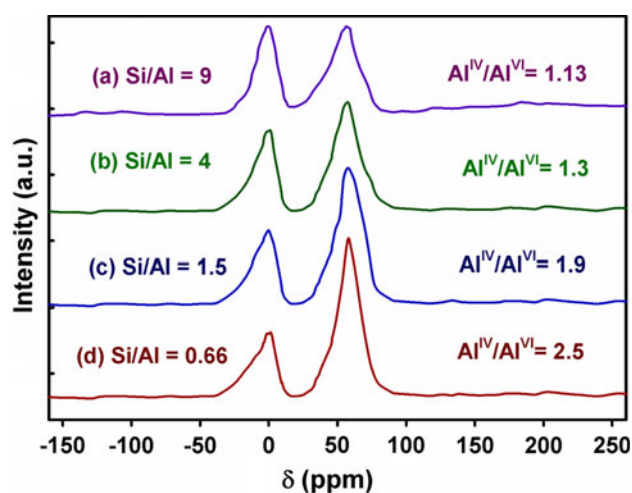
Fig. 2 ^{27}Al MAS NMR spectra of cubic Pm3n aluminosilica adsorbents with Si/Al ratios of 9.0 (*a*), 4.0 (*b*), 1.5 (*c*), and 0.66 (*d*)

Fig. 3 FTIR characteristics of the 3D mesocage aluminasilica adsorbents of proteins with different Si/Al ratios of 9 (*a*), 4 (*b*), 1.5 (*c*), and 0.66 (*d*), respectively

modes [32]. The general features of the OH stretching bands are in the 3,100–3,700 cm^{-1} region. The low resolution bands observed at 1,598–2,982 cm^{-1} range could be assigned to the OH vibrational mode of the hydroxyl molecule, which is observed in almost all the natural hydrous silicates [32]. The doublet at 1,000–1,200 cm^{-1} is due to overlapping Si–O–Si and Al–O–Si stretching vibrations in tetrahedral bridging bonds of aluminosilica adsorbents. The shoulder band at 950–960 cm^{-1} is assigned to Al–OH bending vibrations. Three dominant groups of bands centered near 470, 580 and 825 cm^{-1} are due to internal vibrations of T–O–T (i.e., Si–O, Al–O and Al–O–Si) bridge: rocking, bending and stretching, respectively. These frequencies suggest that the adsorbents exhibit Brønsted acidity between that of silanols and the strong bridging hydroxyl groups, leading to enhanced adsorption amount of proteins.

3.2 Morphological features of mesoporous adsorbent for biomolecules

Figure 4a shows that calcined monoliths attained the stable and tough shape of the as-made sample despite losing transparency because of the high-temperature treatment. SEM images of mesocage cubic *Pm3n* aluminosilica monoliths with low Si/Al ratio as 1.5 show large particle morphologies (ca. 1–5 μm long). The HRSEM images (Fig. 4b–d) reflected irregular-shaped intrapore voids (distributed between 100 nm and 1 μm), which indicated structural surface defects, particularly in samples that contain Al. The development of ultra- or micrometer-sized scale morphology composed of 3D mesoporous monoliths, which can be effectively used to separate large macromolecules, has potential use for biomedical applications. EDX technique proved the *Pm3n* monolith composition;
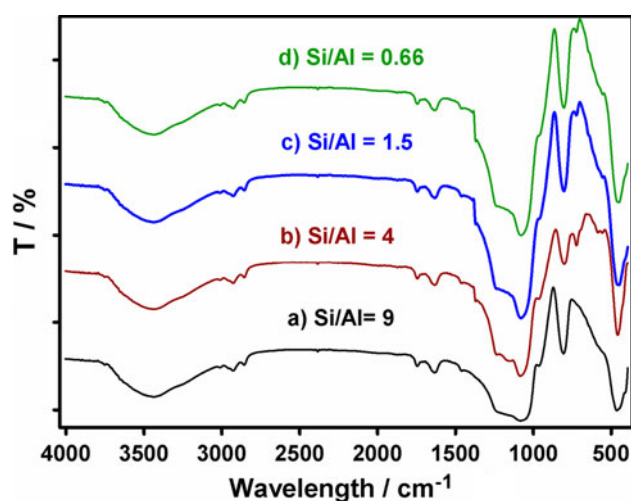
however, the spectrum (Fig. 4d) was recorded over a wide range of domains and on several spots. Overall, EDX analyses revealed the calculated and analyzed values of atomic abundance of O, Al, and Si species that existed in bulk solid monoliths with a Si/Al ratio value equal to 1.5. The results were compatibly averaged with bulk quantities of synthesized *Pm3n* monolith samples regardless of the self-aggregation of Si/Al species.

TEM images of cage cubic *Pm3n* aluminosilica monoliths (with Al/Si ratios of 1.5) that were recorded along [111] and [210] directions indicated well-ordered pores connected to large regions of cubic *Pm3n* aluminosilica monoliths (Fig. 5c, d). These images show that the pores are highly uniform, regular, and ordered. Uniformly sized cage-like pores and 3D lattice crystal of cubic *Pm3n* arrangements of monoliths may facilitate protein diffusion and immobilization during the adsorption process. The interplanar distance estimated from the TEM image agrees with a d$_{210}$ spacing of the diffraction pattern, which indicated the structural integrity of primitive-centered cubic mesoporous structures with Pm3n space groups (Fig. 1A) [27, 28]. Generally, the TEM images indicated that mesoscopic qualities of aluminosilica structures retain their long-range structural ordering over a large area of cubic lattices even for samples with Si/Al ratios of 1.5, which is consistent with XRD patterns [24, 27, 32].

3.3 Mesoporous adsorbent for biomolecules

Scheme 2 shows the simple model structure of mesocage aluminosilicate monoliths as mesoporous adsorbent for adsorption and trapping of proteins from aqueous solution. First, *Pm3n* was synthesized by a direct templating method
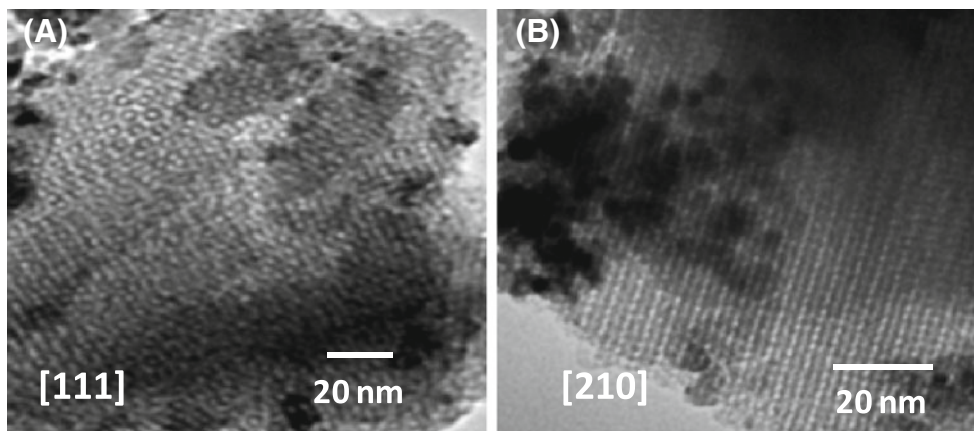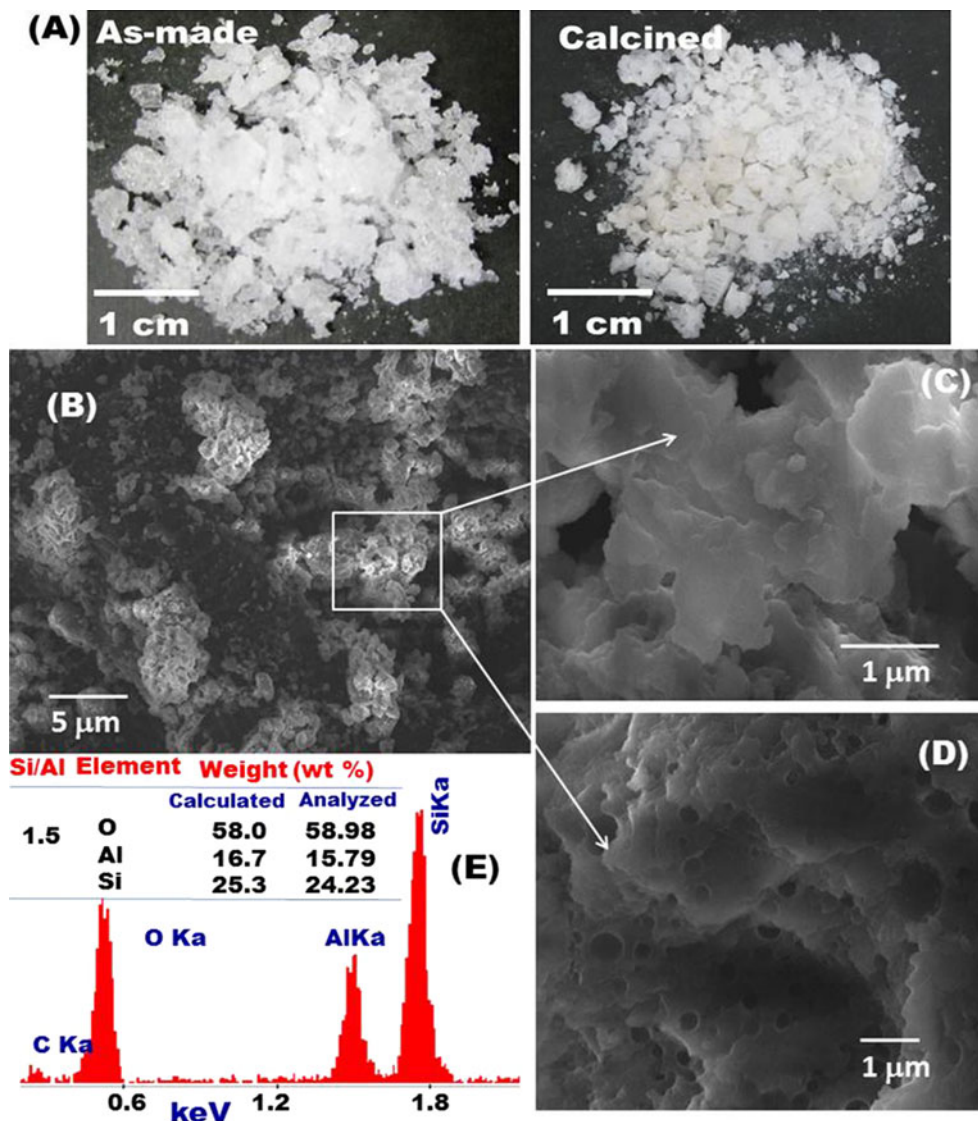
Fig. 5 HR-TEM images of cubic Pm3n aluminosilica (with Si/Al ratio of 1.5) were recorded along the [111] (**a**) and [210] (**b**) zone axes

that involved quaternary microemulsion liquid crystalline phase of reactant composition. The controlled size and fabrication of cubic *Pm3n* mesoporous adsorbents with ratios of $9 \leq$ Si/Al ≥ 0.66 was a key factor in the enhancement of the coverage surfaces and in intra-particle diffusion into the pore architecture (Scheme 2a). All Lewis acid sites may transform into Bronsted acid sites of the aluminosilica adsorbents as a result of direct immobilization of different proteins in an aqueous solution [33–39]. Therefore, the number of Bronsted acid sites for aluminosilicas considers the enhanced adsorption uptake of proteins. Significant factors such as the fabrication strategy of aluminosilicas as well as the nature and amount of incorporated aluminum in the framework matrices control the extent of acidity. Second, size-selective protein adsorption was initiated inside the mesocage and onto pore surfaces of cubic *Pm3n* structures (Scheme 2b). UV–vis spectroscopy revealed the full immobilization and loading capacity of protein molecules onto mesoporous adsorbent monoliths.

3.4 Batch adsorption assays of macromolecules

To evaluate the potential of mesoporous adsorbents, several key factors such as molecular size and concentration of protein as well as the amount of active surface sites of adsorbents were investigated by conducting batch adsorption assays (Fig. 6a, b). The adsorption amount of biomolecules (INS, CytC, LYS, Mb, and β-LG proteins) at the equilibrium step was calculated by the following equation:

$$q_e = (C_o - C_e)V/m$$

where q_e is the adsorption capacity at equilibrium (mol g^{-1}), C_o and C_e are initial and equilibrium concentrations of proteins (mol L^{-1}), respectively, V is the volume of the aqueous solution (L), and m is the mass (g) of the bioadsorbent used in the experiments.

To evaluate the effects of active surface site (center) of the mesoporous aluminosilica adsorbents that have pore cavities within a range from 4.3 to 4.7 nm on protein size-selective adsorption, a series of adsorption assays were conducted using the mesoporous adsorbent synthesized with different Si/Al ratios (from 9 to 0.66) at the same experimental conditions using CytC (2×10^{-5} M) (Fig. 6a). Results indicated that decreased acidity with increased Si/Al ratios significantly affect overall adsorption capacity and kinetics of the CytC protein (Fig. 6a). In this adsorption assay, all Lewis acid sites transform into Bronsted acid sites because of biomolecular adsorption onto the aluminosilica monoliths in aqueous solutions. Biomolecules have a minimal tendency to coordinate with Lewis acid sites. The number of Bronsted acid sites for aluminosilica monolith adsorbents is crucial for enhanced adsorption uptake with high Al content, as evidenced from the low adsorption amount of mesocage silica monoliths (Fig. 6a) [1–3]. The results (see Figs. 2, 6a) show that increased Al^{IV}/Al^{VI} ratios result in enhanced adsorption amount (q_t; mol·g^{-1}) of the proteins. This finding indicates that the proteins may be adsorbed readily onto monoliths that show highly tetrahedral (Al^{IV}, AlO$_4^-$, framework) aluminum sites (Fig. 2).

Figure 6b shows adsorption capacity changes versus time for different proteins (INS, CytC, LYS, Mb, and β-LG) using mesoporous adsorbent monoliths with a Si/Al ratio of 1.5. Three features marked the adsorption assay. First, the induced adsorption period in the order of minutes, which depended on each protein's molecular weight, shape, and size, was distinct. Second, the adsorption rate significantly increased with increased time. Third, saturation of the adsorbed amount at the equilibrium state was observed in S-adsorption curves. Results indicate that the adsorption rate and capacity at equilibrium increased with decreased protein molecular weight and size.

3.5 Kinetic and thermodynamic studies of protein adsorption

The kinetics of adsorption describes the rate of the adsorption process that governs the residence time of protein adsorption assays, and it is essential in defining adsorption efficiency in

Scheme 2 Mesocage aluminosilicate adsorbents (**a**) for protein adsorption from an aqueous solution (**b**). Insets (*bottom*) are TEM images for the adsorbents before and after adsorption. The *design* indicates the feasibility of protein adsorption inside the mesopores of cubic *Pm3n* structures and the full reversibility of the adsorption process (the bar = 20 nm)
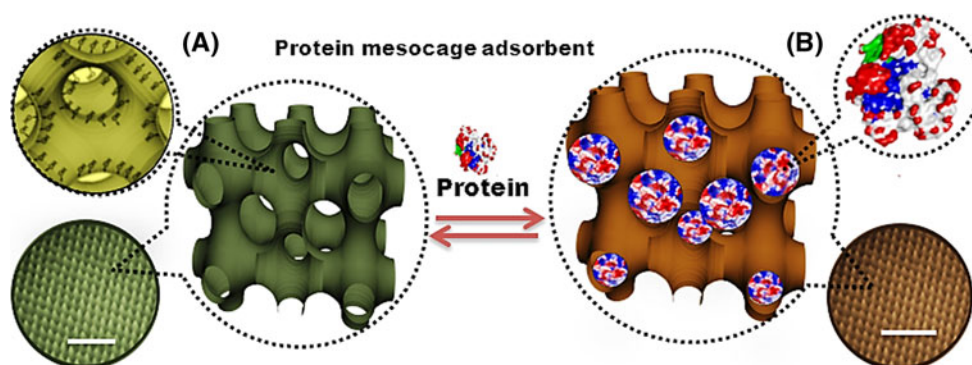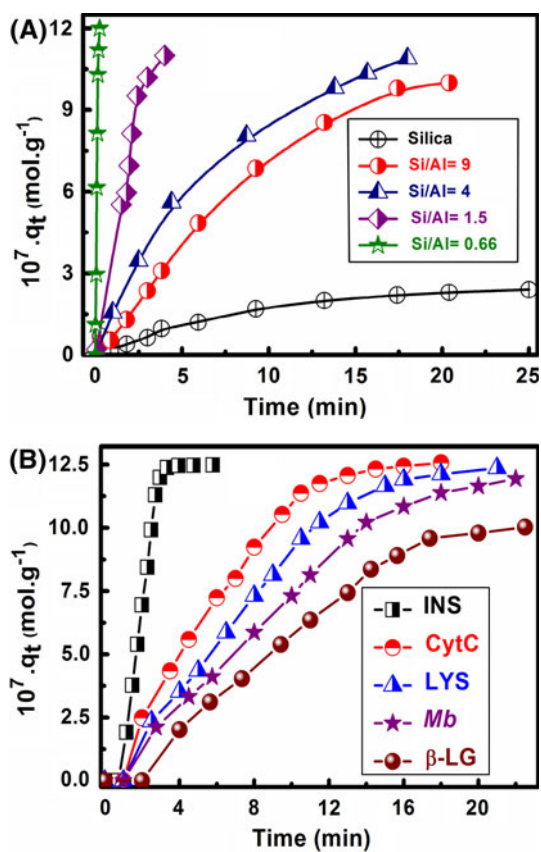
Fig. 6 Time dependence of adsorption amount of proteins onto the mesocage silica and aluminosilica adsorbents (1.6 g L^{-1}). **a** Effect of the Si/Al ratios of bioadsorbents on CytC adsorption (2 × 10^{-5} M). **b** Effect of protein molecular weight and size on the adsorption assays of proteins (1 × 10^{-6} M). **b** Using bioadsorbents with Si/Al ratios of 1.5
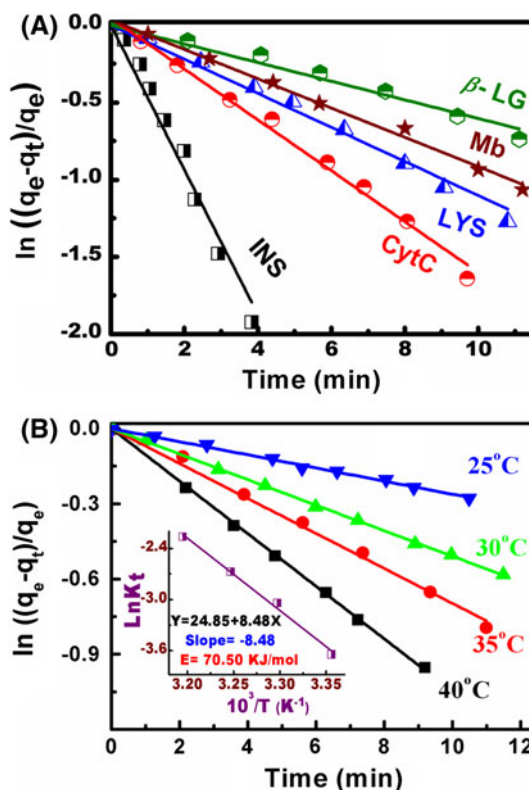

Fig. 7 a Pseudo-first-order kinetics of the adsorbed proteins with different molecular weights and sizes; and **b** Temperature-dependent adsorption and Arrhenius plot (*inset*) of (1 × 10^{-5} mol L^{-1}) Mb adsorbed into (1.6 g L^{-1}) adsorbents with Si/Al ratio of 1.5 at 25 °C

terms of rate and capacity. To investigate the adsorption mechanism, various linear regression equations were proposed based on the adsorption data (see Fig. 6). Our results indicate that linearization in the ln [(q_e–q_t)/q_e] versus t relationship coordinates best describe the experimental adsorption curves (Fig. 7). This finding indicated that the adsorption in solid–liquid systems can be described as pseudo-first-order based on the adsorption capacity of mesobioabent solids. Figure 7a shows that the first-order kinetic equation best describes the data on protein adsorption into mesoporous adsorbents. The values of the rate constant k_t (min^{-1}) of protein adsorption were determined from the slope of the linear first-order kinetic equation. The results of the kinetic studies indicate that k_t values decreased according to the following sequence: INS > CytC > LYS > Mb > β-LG. The k_t values of proteins are consistent with the same sequence of the adsorption amounts of these proteins. Figure 6b shows that k_t increased with increased temperature, indicating that k_t was a temperature-dependent constant. The activation energy E of

protein adsorption was derived from an Arrhenius plot (Fig. 7b inset). Other activation parameters of the free energy of activation, $\Delta G^{\#}$, the enthalpy of activation, $\Delta G H^{\#}$, and the entropy of activation, $\Delta G S^{\#}$, as calculated from Eyring's equation, are listed in Table 1. The adsorbed enzyme requires activation energy to correspond with the adsorption energy of all additional proteins that make contact with the solid surface. Variations in the apparent activation energies for diffusion and transport correspond to changes in protein sizes and concentrations [40]. Our results indicated that the lower E value with higher k_t value agreed with the sequence of the adsorption capacity (q_e mol g^{-1}) of the proteins in the mesoporous adsorbent monoliths (Table 1). The values of the activation parameters were nearly consistent with those reported for the diffusion of small molecules through the interior particle pores of solid adsorbents, which reflected easy protein diffusion into the interior mesoadsorbent monoliths [41–44].

$$\frac{dq}{dt} = k_t(q_e - q_t)$$

Applying the initial conditions $q_t = 0$ at $t = 0$ yields the linear integration form of the pseudo-first-order model as

Table 1 The kinetic and thermodynamic parameters of the adsorption of [1×10^{-6} mol L^{-1}] proteins into (1.6 g L^{-1}) mesoporous adsorbent with Si/Al ratio of 0.66

Protein	T (K)	Kinetic parameters					Thermodynamic			
		k_t (min^{-1})	E (kJ mol^{-1})	ΔH^* (kJ mol^{-1})	ΔS^* (J K.mol^{-1})	ΔG^* (kJ mol^{-1})	K_c	ΔH (kJ mol^{-1})	ΔS (J K.mol^{-1})	ΔG (kJ mol^{-1})
INS	298	0.002	23.85	912.55	97.27	883.5	0.084	129.1	371.57	20.27
	303	0.004				883.1	0.064			18.42
	308	0.006				882.6	0.053			16.56
	313	0.008				882.1	0.040			14.70
CytC	298	0.007	51.27	280.37	88.13	254.1	0.504	93.51	273.11	13.49
	303	0.012				253.7	0.384			12.12
	308	0.017				253.2	0.319			10.76
	313	0.025				252.8	0.240			9.39
LYS	298	0.009	59.48	238.75	86.22	213.1	0.698	76.45	228.37	9.53
	303	0.016				212.6	0.527			8.39
	308	0.022				212.2	0.415			7.25
	313	0.031				211.8	0.312			6.11
Mb	298	0.03	70.50	74.04	77.34	51.02	0.935	67.35	210.75	5.60
	303	0.05				50.06	0.702			4.55
	308	0.06				50.02	0.533			3.50
	313	0.09				49.86	0.399			2.44
β-LG	298	0.03	76.53	68.01	76.49	45.22	1.625	62.03	200.53	3.27
	303	0.05				44.83	1.109			2.27
	308	0.07				44.45	0.807			1.27
	313	0.10				44.07	0.650			0.26

$$Ln(q_e - q_t/q_e) = k_t t$$

$$k_t = \frac{KT}{h} e^{-\Delta G^{\#}/RT}$$

$$\Delta H^{\#} = E - RT$$

$$\Delta G^{\#} = \Delta H^{\#} - T\Delta S^{\#}$$

$$Ln^{k,h}/KT = -\Delta H/RT + \Delta S/R$$

where k is the Boltzmann constant, h is the Planck constant, and T is the absolute temperature.

To investigate the features and stability of protein immobilization into the interior pores of mesoporous adsorbent during adsorption assays, a thermodynamic study was conducted on protein adsorption from 25 to 40 °C. The thermodynamic equilibrium constant K_c that depends on the fractional attainment of equilibrium f_e of the protein-adsorbed molecules was deduced using the following equation:

$$K_c = \frac{q_f}{1 - q_f}$$

where q_f is the ratio of the amount of molecules adsorbed at a time (q_t) to that adsorbed at infinity (q_∞), (i.e., $q_f = q_t/q_\infty$).

From the value of K_c, the Gibbs free energy change, ΔG, can be derived. The plot of ln K_c versus $1/T$ gives the numerical values of ΔH of the adsorption of protein adsorption. ΔG and ΔS are obtained by the following relations:

$$\Delta G = -RTLnK_c$$

$$LnK_c = -\Delta H/RT + \Delta S/R$$

where ΔH, ΔS, and ΔG are the changes in enthalpy, entropy, and Gibbs free energy; T is the temperature in Kelvin; R is the gas constant; and K_c is the equilibrium constant.

Table 1 presents the calculations of ΔH, ΔG, and ΔS. The thermodynamic equilibrium constant K_c increased with the temperature for all protein adsorption assays, whereas the absolute value of ΔG increased with decreased temperature. This result indicated that adsorption was spontaneous and tended to occur at a high temperature, which confirmed that protein immobilization underwent an endothermic adsorption process. The ΔS values also increased in the order INS > CytC > LYS > Mb > β-LG, thereby contributing to a greater value of K_c and greater stability of thermodynamic adsorption. Thus, attraction existed between the proteins and active acid sites in the micrometer-sized monolith particle, which caused the proteins to diffuse toward the particle center.

Fig. 8 Langmuir adsorption isotherms (**a**) and the linear form of the Langmuir plot (**b**) for protein adsorption into (1.6 g L^{-1}) adsorbent with Si/Al ratio of 9 at 25 °C
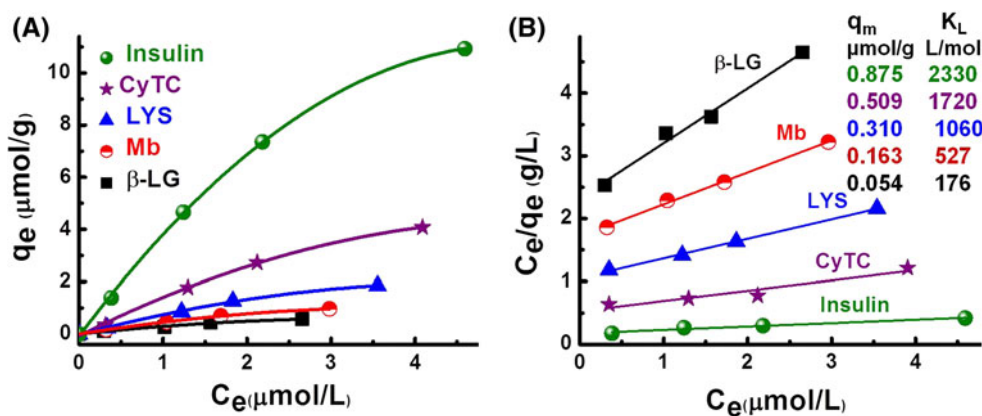
3.6 Protein adsorption isotherms

To study the adsorption isotherm of proteins in an aqueous solution using monoliths, the Langmuir isotherm model at equilibrium was applied as a theoretical model for monolayer adsorption. The monolayer coverage of proteins onto mesoporous adsorbent surfaces at constant temperature is represented by the Langmuir isotherm (Fig. 7). The adsorption characteristics of protein molecules onto the adsorbents can be studied by the Langmuir isotherm equation as follows [32, 45]:

$$C_e/q_e = 1/(K_L q_m) + (1/q_m)C_e$$

where q_m (mmol g^{-1}) is the amount of protein molecules adsorbed to form a monolayer coverage and K_L is the Langmuir adsorption equilibrium constant. The results revealed increased adsorption amount of proteins into adsorbents with increased concentration at equilibrium (Fig. 8a). The straight line of the C_e/q_e versus C_e plot (Fig. 8b) represented the formation of the monolayer coverage of proteins in the interior pore surfaces of monoliths as a result of adsorption assay. The linear adsorption curves indicated that a wide range of concentrations of biomolecules can be removed from an aqueous solution by a one-step treatment. A linear graph (Fig. 8b) with a correlation coefficient range of 0.98–0.99 clearly showed that the Langmuir adsorption isotherms were characteristic of the adsorption assays for all proteins. The monolayer adsorption capacity q_m and the Langmuir coverage constant K_L were obtained from the slope and intercept of the linear plot. The q_m and K_L values decreased in the order β-LG < Mb < LYS < CytC < INS. This tendency was consistent with the adsorption sequence of protein, as shown in Fig. 6b.

Fraction of the coverage mesoporous adsorbent pore surfaces (f_c, g/m^2) occupied by the protein molecules were calculated by the following equation:

$$f_c = \mathcal{M}\beta/S$$

where M is the molecular area of the protein molecule, S (m^2 g^{-1}) is the surface area of monoliths, and β is the
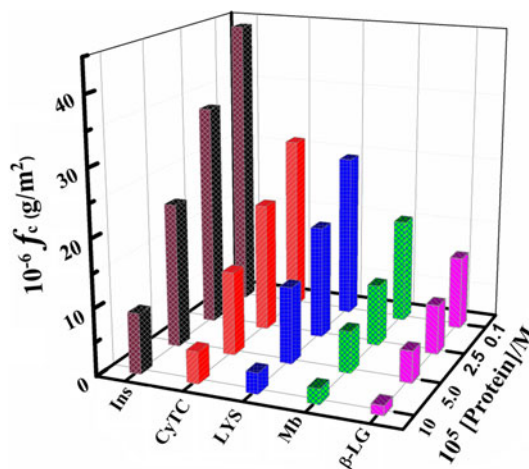

Fig. 9 Fraction of the coverage of mesoporous proteins based on fabricated monoliths with Si/Al ratios of 1.5

number of molecules adsorbed per unit area of the mesoporous adsorbent. However, β can be calculated as follows: $\beta = q_e N_A/S$, where N_A is Avogadro's number. Coverage surface f_c of proteins was significantly affected by active functional acid sites. However, the f_c value decreased with high molecular weight and protein concentrations, as shown in Fig. 9.

3.7 Reusability of mesoporous adsorbent monoliths

Synthesized mesoporous adsorbents have limited applications in medicine because of their low pore density and non-uniform pore size within reuse cycles. A major advantage of mesoporous adsorbent monoliths is their reducibility and reversibility after multiple adsorption cycles. Figure 10 shows that the monoliths retain high protein adsorption efficiency after undergoing a number of reuse cycles such as dead-end adsorption [27, 46]. Clogging of pores by proteins is another issue that needs to be addressed. Song et al. [30] reported the use of a self-cleaning process to handle membrane pores that are
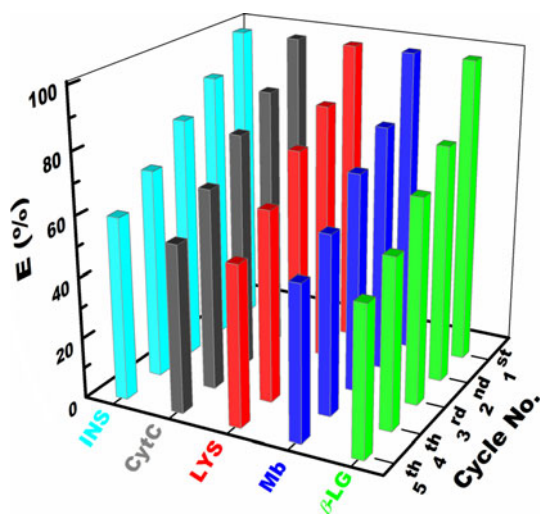
Fig. 10 Reusability study of (1×10^{-6} M) protein adsorption assays using mesoporous adsorbent monoliths with Si/Al ratios of 1.5. The efficiency (E %) of the adsorbent was calculated from the % ratio of recovery concentration uptake (U_R) per reuse cycle (No.) and the initial concentration uptake (U_o) obtained from the initial use of the adsorbent monoliths

clogged with macromolecules. In the current work, the reversible adsorption process was conducted by a simple chemical treatment based on an acidified solution (HCl/NaCl) to effectively remove proteins trapped in the monolith pores without causing significant damage to the texture and physical properties of the mesostructures. A pH 2 buffer solution (HCl/NaCl) was used to effectively remove adsorbed biomolecules from the mesoporous adsorbents. The mesoporous adsorbents were washed several times to ensure that they were thoroughly clean, which was proved by a solid UV–vis spectroscopy. Our experimental findings show that during the cleaning process, proteins with a high molecular size and weight took a longer time to be removed from the interior monoliths.

Therefore, the efficiency of the adsorbent monoliths during the reuse cycles of adsorption assays of proteins decreases in the order β-LG < Mb < LYS < CytC < INS, which indicated the effect of protein size, shape, and weight in continuous dead-end adsorption. Generally, the results (Fig. 10) indicated the reversibility of the adsorption process of proteins, as shown by the Langmuir adsorption model, which assumed a reversible process. To confirm a favorable adsorption/desorption process, kinetic studies of the desorption rate of the trapped proteins in the adsorbent were conducted (Fig. 10). The adsorbed proteins were found to desorb slowly when exposed to a buffer solution (HCl/NaCl). The desorption rates appear to be influenced by protein–alumina pore surface interactions and the molecular weight of proteins. The lack of desorption rate indicated that desorption process mainly occurred from the interior cavities of trapped proteins (Fig. 11). Our results indicated that the Langmuir equilibrium constant K_L values were consistent with the ratio of adsorption/desorption rates of proteins (k_1/k_{-1}). Thus, the protein adsorption assays were fully reversible (Fig. 11).

To investigate the effect of aluminium contents (i.e., Si/Al ratios) of adsorbents on the protein release, we carried out a series of protein adsorption efficiency with five times of reuse cycle. In this reusable adsorption assay, the % ratio of recovery concentration uptake with each reuse cycle was compared with that of the initial concentration uptake of the adsorbents before using an acidified solution (HCl/NaCl) eluent (Fig. 12). Our finding indicated that significant changes in the adsorbent affinity toward the proteins from aqueous solution were dependent on the Si/Al ratios after several release cycles. For the adsorbents with low Si/Al ratio (0.66), the decrease in adsorption efficiency with reuse cycles was much greater than that at high Si/Al ratios. These results indicated that with high Al doping of the monoliths, the enhancement of binding
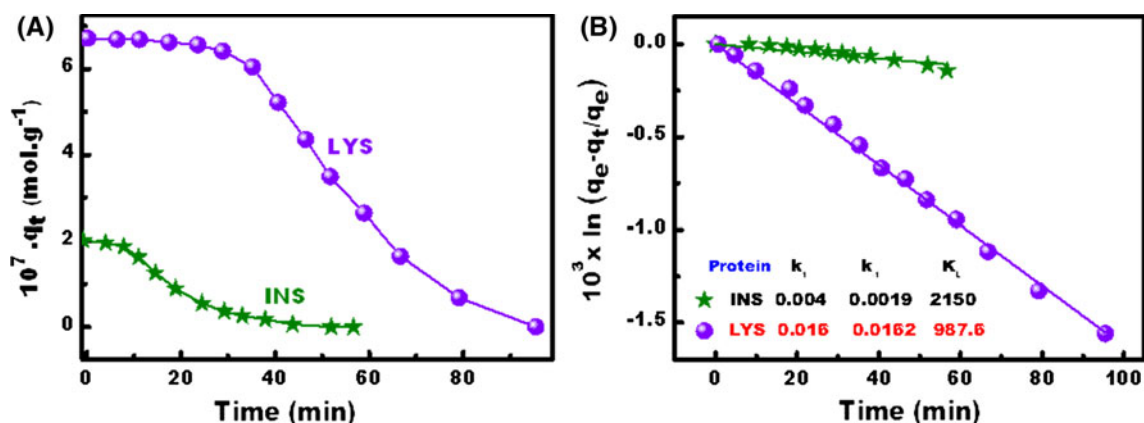

Fig. 11 Desorption profile of proteins from mesoporous adsorbents (**a**) and the rate of desorption (**b**). The release of protein from a mesoporous adsorbent was achieved by applying a mixture of HCl/NaCl
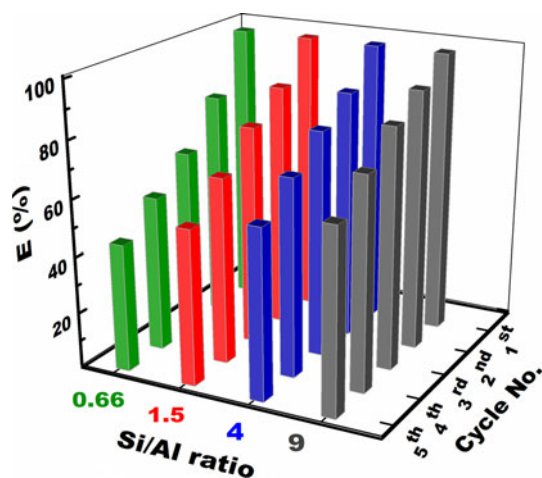
Fig. 12 Study the effect of Si/Al ratios of aluminosilica adsorbents on the $(1 \times 10^{-6}$ M) Cyt*C* release as a function of Cyt*C* adsorption efficiency with five times of reuse cycle

surface coverage of the adsorbents increases the protein absorptivity and the difficulty of removing the proteins by the eluent.

4 Conclusions

Mesoporous protein adsorbents have been extensively studied for decades because of their importance in a wide range of applications such as biochemistry, diagnostic assays, gene technology, and pharmaceutical sciences. We designed spherical 3D mesoporous adsorbent-based pore cavities of monoliths to achieve efficient adsorption of INS, Cyt*C*, LYS, Mb, and β-LG proteins. The properties of mesoporous adsorbents can potentially enhance the coverage of the protein molecules adsorbed onto adsorbent pore surfaces. Despite the challenging optimization of the reducibility and reversibility of the adsorbents, the protein adsorption efficiency of monoliths was attained after a number of reuse cycles, which indicates that mesoporous adsorbents are significant to the process. A successful protein separation design that uses such mesoporous materials shows potential in bioanalytical applications.

References

1. F. Bellezza, A. Cipiciani, L. Latterini, T. Posati, P. Sassi, Langmuir **25**, 10918 (2009)
2. J. Deere, E. Magner, J.G. Wall, B.K. Hodnett, Chem. Commun. **5**, 465 (2001)
3. A. Zukal, J. Mayerova, J. Cejka, Phys. Chem. Chem. Phys. **12**, 5240 (2010)
4. Z. Liu, M. Li, X. Yang, M. Yin, J. Ren, X. Qu, Biomaterials **32**, 4683 (2011)
5. J.D. Andrade, V. Hlady, A.P. Wei, Pure Appl. Chem. **64**, 1777 (1992)
6. T.-Y. Ma, X.-J. Zhang, Z.-Y. Yuan, J. Phys. Chem. C **113**, 12854 (2009)
7. S.A. El-Safty, M. Khairy, M. Ismael, H. Kawarada, Appl. Catal. B **123–124**, 162 (2012)
8. S.A. El-Safty, M. Khairy, M. Ismeal, Sens. Act. B. **166–167**, 253 (2012)
9. S.B. Hartono, S.Z. Qiao, K. Jack, B.P. Ladewig, Z. Hao, G.Q. Lu, Langmuir **25**, 6413 (2009)
10. I.S. Lee, N.Y. Lee, J. Park, B.H. Kim, Y.W. Yi, T. Kim, J. Am. Chem. Soc. **128**, 10658 (2006)
11. X. Liu, T. Peng, J. Yao, H. Lv, C. Huang, J. Solid State Chem. **183**, 1448 (2010)
12. P. Kim, J.B. Joo, H. Kim, W. Kim, Y. Kim, I.K. Song, J. Yi, Catal. Lett. **104**, 181 (2005)
13. Z. Xu, S.-L. Wang, H.-W. Gao, J. Hazard. Mater. **180**, 375 (2010)
14. M. Lundqvist, I. Sethson, B.H. Jonsson, Langmuir **20**, 10639 (2004)
15. A.A. Vertegel, R.W. Siegel, J.S. Dordick, Langmuir **20**, 6800 (2004)
16. B. Menaa, C. Torres, M. Herrero, V. Rives, A.R.W. Gilbert, D.K. Eggers, Biophys. J. **95**, L51–L53 (2008)
17. S.A. El-Safty, Trends Anal. Chem. **30**, 447 (2011)
18. S.A. El-Safty, M.A. Shenashen, Anal. Chim. Acta **694**, 151 (2011)
19. S.A. El-Safty, A. Shahat, Md.R. Awual, M. Mekawy, J. Mater. Chem. **21**, 5593 (2011)
20. J.J. Chiu, D.J. Pine, S.T. Bishop, B.F. Chmelka, J. Catal. **221**, 400 (2004)
21. A. Galarneau, J. Iapichella, K. Bonhomme, F.D. Renzo, P. Kooyman, O. Terasaki, F. Fajula, Adv. Funct. Mater. **16**, 1657 (2006)
22. S.A. El-Safty, J. Porous Mater. **18**, 259 (2011)
23. Y. Sakamoto, M. Kaneda, O. Terasaki, D.Y. Zhao, J.M. Kim, G.D. Stucky, H.J. Shin, R. Ryoo, Nature **408**, 449 (2000)
24. J.R. Matos, M. Kruk, L.P. Mercuri, M. Jaroniec, L. Zhao, T. Kamiyama, O. Terasaki, T.J. Pinnavaia, Y. Liu, J. Am. Chem. Soc. **125**, 821 (2003)
25. P.I. Ravikovitch, A.V. Neimark, Langmuir **18**, 9830 (2002)
26. M. Thommes, B. Smarsly, M. Groenewolt, P.I. Ravikovitch, A.V. Neimark, Langmuir **22**, 756 (2006)
27. S.A. El-Safty, T. Hanaoka, Chem. Mater. **16**, 384 (2004)
28. S.A. El-Safty, T. Hanaoka, Adv. Mater. **15**, 1893 (2003)
29. S.A. El-Safty, A. Shahat, W. Warkocki, M. Ohnuma, Small **7**, 62 (2011)
30. Y.-Y. Song, F. Schmidt-Stein, S. Berger, P. Schmuki, Small **6**, 1180 (2010)
31. S.A. El-Safty, T. Balaji, H. Matsunaga, T. Hanaoka, F. Mizukami, Angew. Chem. Int. Ed. **45**, 7202 (2006)
32. J.A. Gadsen, *Infrared Spectra of Minerals and Related Inorganic compounds* (Butterworths, London, 1975)
33. X. Liu, T. Peng, J. Yao, H. Lv, C. Huang, J. Solid State Chem. **183**, 1448 (2010)
34. P. Kim, J.B. Joo, H. Kim, W. Kim, Y. Kim, I.K. Song, J. Yi, Catal. Lett. **104**, 181 (2005)
35. A.R. Garcia, R.B. de Barros, A. Fidalgo, L.M. Ilharco, Langmuir **23**, 10164 (2007)
36. K.J. Klabunde, R.M. Richards, *Nanoscale Materials in Chemistry* (Wiley, London, 2009)
37. C. Marquez-Alvarez, N. Zilkova, J. Perez-Pariente, J. Cejka, Catal. Rev. **50**, 222 (2008)
38. N. Bejenaru, C. Lancelot, P. Blanchard, C. Lamonier, L. Rouleau, E. Payen, F. Dumeignil, S. Royer, Chem. Mater. **21**, 522 (2009)
39. M.N. Timofeeva, V.N. Panchenko, A. Gil, Y.A. Chesalov, T.P. Sorokina, V.A. Likholobov, Appl. Catal. B Environ. **102**, 433 (2011)
40. B. Chazotte, C.R. Hackenbrock, J. Biol. Chem. **264**, 4978 (1989)
41. D.R. Rolison, Science **299**, 1698 (2003)

42. J.J. Pignatello, B. Xing, Environ. Sci. Tech. **30**, 1–11 (1996)
43. B.C. Pan, F.W. Meng, X.Q. Chen, B.J. Pan, X.T. Li, W.M. Zhang, X. Zhang, J.L. Chen, Q.X. Zhang, Y. Sun, J. Hazard. Mater. **124**, 74 (2005)
44. R. Hahn, P. Bauerhansl, K. Shimahara, C. Wizniewski, A. Tscheliessnig, A. Jungbauer, J. Chromatogr. A **1093**, 98 (2005)
45. A. Gil, A. Diaza, M. Montes, D.R. Acosta, D.F. Mexico, J. Mater. Sci. **29**, 4927 (1994)
46. B. Balannec, M. Vourch, M. Rabiller-Baudry, B. Chaufer, Sep. Purif. Technol. **42**, 195 (2005)